Contents

1 Design & Simulation

The aim of this work is to design and test a miniaturized OCT microscope as a component of a multi-modal endoscope. As described in section 1.3, this probe consist of two spectrally-separated optical paths that run partially in parallel through a micro-optical bench system. This approach allows independent tuning of the optical parameters of the two imaging modalities – such as the numerical aperture (NA) or depth of field – while still providing a geometrical overlap of the two acquired images. An integrated tubular piezoelectric fiber scanner is used to perform en face scanning required for three dimensional OCT measurements. This scanning engine has an outer diameter of 0.9 mm and a length of 9 mm, and features custom fabricated 10 µm thick polyimide flexible interconnect lines to address the four piezoelectric electrodes.

The following section describes the conception and design of the endoscope, starting from the medical and geometrical requirements, through analytical modeling and towards the optimization of each component.

1.1 Design Requirements

The OCT microscope should fulfill the following requirements:

Mechanical Requirements

- The scanner, electrical connections and optics should fit in channel with a $1\,\mathrm{mm} \times 1\,\mathrm{mm}$ cross section located in the lower level of the multimodal bench. This way the total cross section of the endoscope can be kept under $3 \times 2\,\mathrm{mm}^2$).
- Its length should be minimized to allow the movement of the endoscope head inside the body.
- The field of view should be maximized for a 2 mm diameter objective lens, which is shared with the endomicroscopy beam path.
- The scanning speed should be adequate for the sampling rates characteristic of SD-OCT ($\sim 100\,\mathrm{kHz}$).

Optical Requirements

- The microscopy and OCT imaging fields should be coaxial to avoid parallax errors.

- The OCT field should be distal-side telecentric to avoid field curvature distortions and to maximize the collection of backscattered light upon normal incidence to the tissue.
- The lateral resolution and depth of field should be adequate for OCT i.e. with numerical aperture ranging from 0.02 to 0.05.
- The backreflections inside the probe should be minimized to avoid any loss of contrast and penetration depth.

1.2 Design overview

The main challenge of this work is to design a scanning mechanism compact enough to be placed in a thin, buried channel of a multimodal probe. Although it is theoretically possible to keep a scanner at the proximal end of the endoscope and use a coherent fiber bundle (CFB) as a relay, there are inherent drawbacks of this method, such as low light throughput, cross-talk and mechanical rigidity [1].

Another challenging requirement is the superposition of the images acquired by the different modalities. If the optical axes are not coaxial, the fields will be shifted and tilted due to parallax error — which gains importance at the small working distances common in endoscopy.

To overcome these problems, and taking into account the above-mentioned requirements, we propose a design based on the HYAZINT multimodal probe [2]. By creating a two layer microbench, it is possible to bury the OCT resonant fiber scanner in the bottom level and keep the rest of the optics together with a beamsplitter to merge both modalities in the top level. An schematic of this mechanism can be seen in Figure 1.1.

The base of the microbench with dimensions of $13 \times 2 \times 1\,\text{mm}^3$ is realized by standard silicon bulk micromachining. On the top layer, the bench accommodates the full field imaging optics that consists of a dichroic beamsplitter cube with dimensions of $2 \times 2 \times 2\,\text{mm}^3$ to separate the two beam paths and two plano-convex lenses with 2 mm diameter, which form the full field microscope. To achieve a highly compact opto-mechanical design, the components of the OCT beam path are buried within a cavity in the base of the micro bench. On the bottom layer a gradient index lens (GRIN lens) with a diameter of 350 µm is directly glued to the tip of a 80 µm single mode fiber to collimate the infrared light of the OCT system with a center wavelength of $\lambda_o = 1311\,\text{nm}$ and a bandwidth of $\Delta\lambda = 90\,\text{nm}$. A spiral scanning of the OCT beam path is achieved by an angular scanner implemented using a piezoelectric tube actuator.

This actuator, called resonant fiber scanner, is able to scan a collimated beam by more than $\pm 5°$ by mechanically amplifying the subtle vibration of a piezoelectric actuator. An objective lens then focuses the beam on the tissue and transforms the angular displacement into translation. By driving the scanner in two axes with two

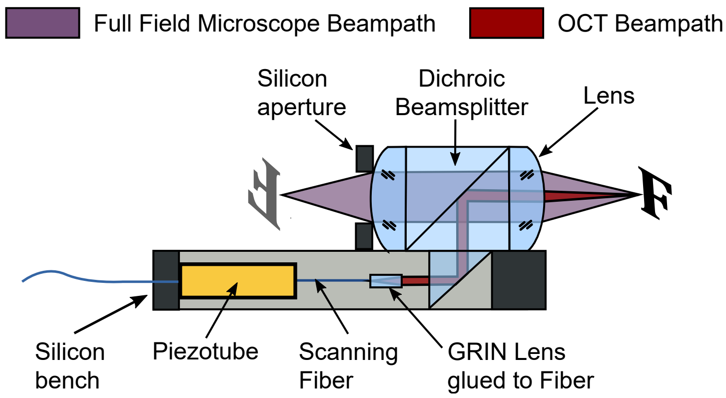

Figure 1.1: Schematic of the MEMS endomicroscope. Two glass lenses glued directly to the dichroic beamsplitter cube form the full field microscopy beam path. A silicon aperture is used to reduce the spherical aberrations. Buried beneath the full field optics, a single mode fiber glued to a collimating GRIN lens forms the OCT channel. The single-mode fiber is fixed in a piezoelectric tube to create a fiber scanner enabling 3D OCT. A reflecting micro-prism glued to a dichroic beamsplitter cube combines the two beam paths.

sinusoids with different phases, it is possible to sample a 2D area of the object in a spiral fashion, as explained in detail in Section 1.3.

The rest of this chapter shows the design and development of the OCT imaging path for the multi-modal probe. However, in order to independently test the behavior of the OCT scanner and optics, a single modality probe was fabricated as a demonstrator. Both systems are mechanically and optically equivalent – the only difference is the presence of the beam splitter.

For completeness, both multi-mode and single-mode optical systems are described.

1.3 Optical Design of the OCT beam path

This section explains in detail the design of the OCT optics and its scanning mechanism. Starting with the concept of Fourier plane scanner, the most relevant design equations are derived, which guide the selection of the optical components to achieve the desired performance, eventually verified by optical simulation.

1.3.1 Fourier Plane Scanner

The OCT beam path is designed as an object-sided telecentric system to avoid distortions in the 3D OCT measurement. To achieve this, the fiber scanner is driven with small angles and is positioned such that the lateral and angular movement of the scanner imitates the beam angles that can be observed in the collimated region of a classical telecentric lens system. Figure 1.2 illustrates this approach. The whole scanner is buried in a channel with a inner diameter of 1 mm limiting the movement of the scanner to a maximum angle θ of 5° that allows a maximum FOV of 1 mm of the OCT beam path.

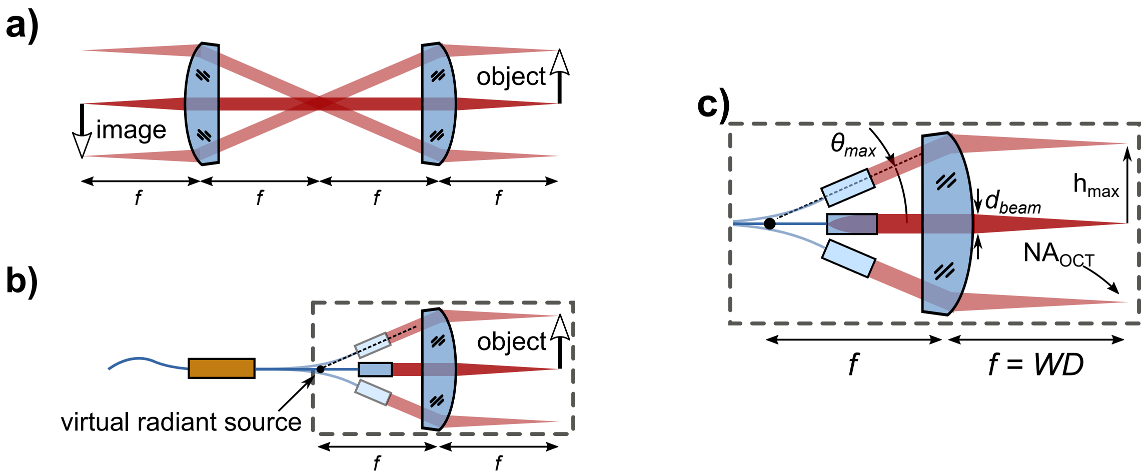

Figure 1.2: **a)** Illustration of a classical telecentric system. The height of the object is translated into an angle θ in the collimated region between the two lenses. This angle is again translated into a corresponding image height by the second lens. **b)** Illustration of the OCT beam path using a fiber scanner in first resonance mode without micro prism and BS. The movement of the GRIN lens due to the fiber scanner and the distance between the GRIN lens and the focusing lens creating the same optical behavior as it can be observed in a classical object sided telecentric system.
c) Nomenclature used in this work.

For the scanner to work as a Fourier plane scanner, at any point of the oscillation the output beam from the GRIN lens should point to a fixed virtual radiant source. This is fulfilled if the bending shape of the scanner is linear with the amplitude and thus, the ratio of the GRIN lens angle to its vertical displacement is kept constant $y = d \cdot \tan\theta \simeq d \cdot \theta \Rightarrow \frac{\theta}{y} = const$ (refer to Figure 1.3).

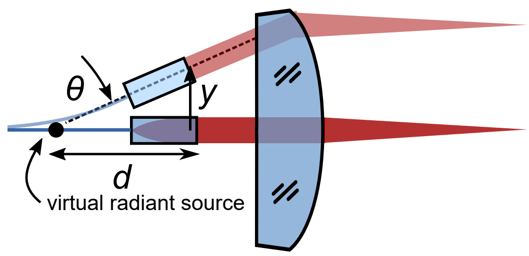

Figure 1.3: Schematic of the Fourier plane scanner at rest and at an arbitrary position with amplitude θ. If the scanner behaves linearly, the output beam will appear to come from a fixed virtual radiant source regardless of the scanning amplitude.

In a Fourier plane scanner, the numerical apertures and focal lengths of the scanning and objective lens are related by the diameter of the beam in the intermediate region between both lenses. Thus, following the schematic of Figure 1.2c, following geometrical optics relations are obtained: $d_{\text{beam}} \simeq 2 \cdot f_{\text{GRIN}} \cdot NA_{\text{fiber}}$ and $d_{\text{beam}} \simeq 2 \cdot f_{\text{obj}} \cdot NA_{\text{OCT}}$. By combining them together the main design equation for the scanner appears:

$$f_{\text{GRIN}} \cdot NA_{\text{fiber}} = f_{\text{obj}} \cdot NA_{\text{OCT}} \tag{1.1}$$

Note that these equations use a small angle approximation valid for small NA: $\tan[\sin^{-1}(NA)] \simeq NA$. In this case, as any NA is smaller than 0.25, the error of this simplification is smaller than 2%.

1.3.2 Component Selection

The design equations that were obtained in the previous section relate all the optical components together. Therefore, once the desired NA is chosen, there is only a free variable available. In this case, the major constraint is given by the commercial availability of the single mode fiber, so the selection of the rest of the components will follow from it.

The only commercially available single mode fiber working in our wavelength range and with thinned cladding diameter (refer to Section 1.4) is *Thorlabs SM980G80*, with a diameter of 80 µm and with $NA_{\text{fiber}} = 0.18$ at 1.33 µm.

In order to collimate the output from the fiber without clipping the gaussian beam, a GRIN lens with an NA_{GRIN} higher than NA_{fiber} is needed. A good fit from the GRINTECH catalog is *GT-LFRL-035-024-20-CC (1550)*, with an $NA_{\text{GRIN}} = 0.20$ and $f_{\text{GRIN}} = 0.91\,\text{mm}$.

Now, by using the relation in Equation 1.1 we can design $f_{\text{objective}}$ by choosing an adequate NA_{OCT}. To preserve a high depth of field (DOF), allow enough space for the beamsplitter and a long working distance, a narrow NA_{OCT} is is preferred – in the range of 0.020 - 0.025. By choosing an intermediate NA_{OCT} of 0.022, the focal length of the objective lens

$$f_{\text{obj}} = f_{\text{GRIN}} \frac{NA_{\text{fiber}}}{NA_{\text{OCT}}} = 0.91\,\text{mm} \frac{0.18}{0.022} = 7.5\,\text{mm} \tag{1.2}$$

can be selected. As one of the facets of the lens has to be cemented to the beamsplitter cube, it is fabricated as a plano-convex spherical lens by *Optik+*.

The field of view (FOV) of the OCT modality can be now calculated considering the maximum angular deflection of the GRIN lens in the tip of the scanning fiber by

$$h_{\max} = f_{\text{obj}} \cdot \tan\theta_{\max} = 7.5\,\text{mm} \cdot \tan 5° = 0.66\,\text{mm} \tag{1.3}$$

equivalent to a FOV of 1.2 mm for a $\theta_{\max}$ of ±5° (section 1.4).

1.3.3 ZEMAX Simulation

Once the components are selected, it is possible to validate the theoretical analysis of the optical design by performing a raytracing simulation. Using ZEMAX, the fiber facet is modeled as the waist of a gaussian beam source, the GRIN lens is modeled using a design file from the manufacturer and the prism, beamsplitter and planoconvex lens are modeled geometrically according to the provided mechanical drawings. The result is shown in Figure 1.4.

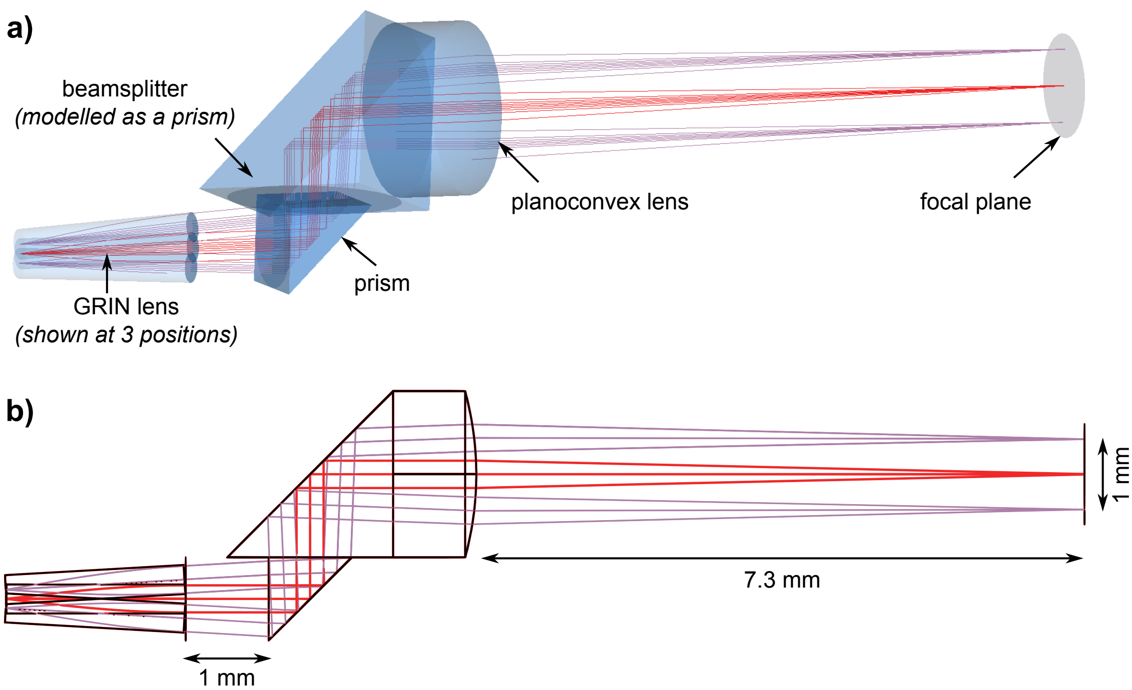

Figure 1.4: **a)** 3D ZEMAX raytracing of the OCT beam path for the center (red rays) and marginal (purple rays) position of the GRIN lens. Note that as the OCT beam path is reflected in the hypotenuse of the beamsplitter, it can be modeled as a 45° prism. **b)** Cross section of a) showing the most relevant dimensions.

The three overlapping rectangles on the left simulate the rest position (red) and maximum deflection (purple) of the GRIN lens. The gap between GRIN lens and prism is calculated so that the focus of the planoconvex lens coincides with the virtual radiant source of the scanner.

Due to the low NA_{OCT} and the good optical quality of the GRIN and planoconvex lenses, the aberrations in this design are negligible and thus has an optical performance close to the diffraction limit. Figure 1.5 proves this behavior by comparing the MTF (Modulation Transfer Function) of an ideal optical system with the simulated MTF of the system which is described.

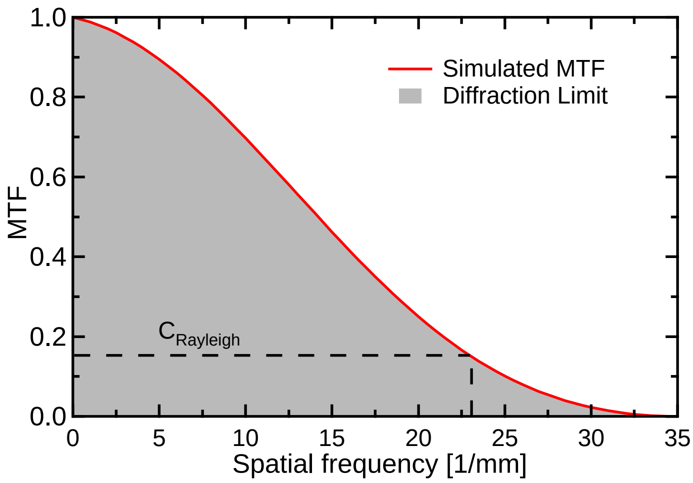

Figure 1.5: Simulated MTF curve of the OCT beam path for the bimodal probe. It can be seen that the system is diffraction limited and provides a lateral resolution of 23.3 lp/mm or 43 µm.

1.3.4 Minimization of backreflections

After the raytracing simulation of the optical system is performed, there is still an important factor to consider: the backreflections inside the probe. In Fourier Domain OCT, any backreflection inside the probe increases the background intensity at the spectrometer, thus limiting its dynamic range. The consequences are higher noise, lower penetration depth and lower contrast of the resultant image. Therefore any source of backreflections in the design should be carefully considered and minimized. The main ones are marked in Figure 1.6 and explained in the following list:

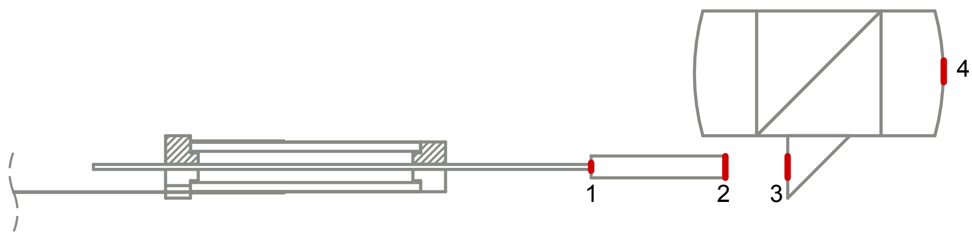

Figure 1.6: Schematic of the multimodal probe showing the main sources of backreflections inside the probe (red). 1) Fiber - GRIN. 2) GRIN - gap. 3) Gap - prism. 4) Objective - air.

1. **Fiber - GRIN interface:** Starting from the proximal side, the facet of the fiber and the GRIN lens are two parallel glass surfaces separated by a small gap. Although the beam is not collimated in this region, a small portion of light can be coupled back to the fiber. In order to minimize any backreflections,

fiber and GRIN are glued together using a refractive-index-matched optical adhesive (*NOA 76*, from *Norland Products*). This way there is no glass to air interface and the maximum refractive index step is reduced to 0.05.

2. **GRIN - gap interface:** The next interface is the distal facet of the GRIN lens. This is the most critical situation – regardless of the scanning angle, there is normal, collimated light incidence. To avoid this problem without resorting to delicate and expensive antireflection coatings, the GRIN lens is manufactured with a 1° tilt exit facet. According to geometrical optics, this tilt induces a vertical shift in the position of the backreflected focal point $\Delta y = f\tan(2\alpha)$ which in this system equates to $0.91\,\mathrm{mm} \cdot \tan(2°) = 31\,\mu\mathrm{m}$.

   The result is visible in the simulation from Figure 1.7: the backreflected light is focused back 31 µm away, effectively missing the core of the fiber – which has a diameter inferior to 5 µm.

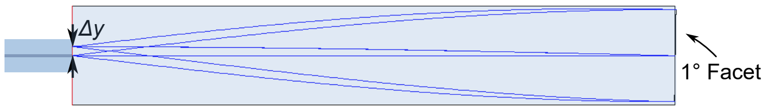

Figure 1.7: Schematic showing the raytracing simulation of a beam exiting from the distal facet of the fiber and being coupled into a GRIN lens with a tilted exit facet. Thanks to it, the backreflected light misses the core of the fiber and is thus not coupled back to the OCT system.

3. **Air - prism interface:** Due to collimated incidence, this interface can produce important backreflections, but only in the resting position of the GRIN lens, when the free end of the GRIN lens is pointing perpendicular to the surface of the prism. To minimize reflections in this situation it is possible to resort to anti-reflection coatings in the facet of the prism.

4. **Objective lens - air interface:** After the prism, the beamsplitter and objective lens are cemented together, making any backreflections negligible. The objective lens has an interface with air, but has an anti-reflection coating on this surface. Furthermore, due to the curved surface of this lens, the backreflected light won't be focused back in the single mode fiber significantly.

Taking these considerations into account, the backreflections were kept below 0.02% in all the manufactured probes, as detailed in **??**.

1.3.5 Single Modality Probe

As stated in the Design Overview, in order to independently test the behavior of the OCT scanner and optics, a single modality probe was fabricated as a demonstrator. Its optical design, depicted in Figure 1.8, emulates the multimodal design from

Figure 1.4 by unfolding its optical path. The main difference is the lack of the prism and beamsplitter and the orientation of the planoconvex lens, which has now with its convex surface facing the GRIN lens to reduce the backreflections which would happen in the case of normal incidence in the planar side of the lens.

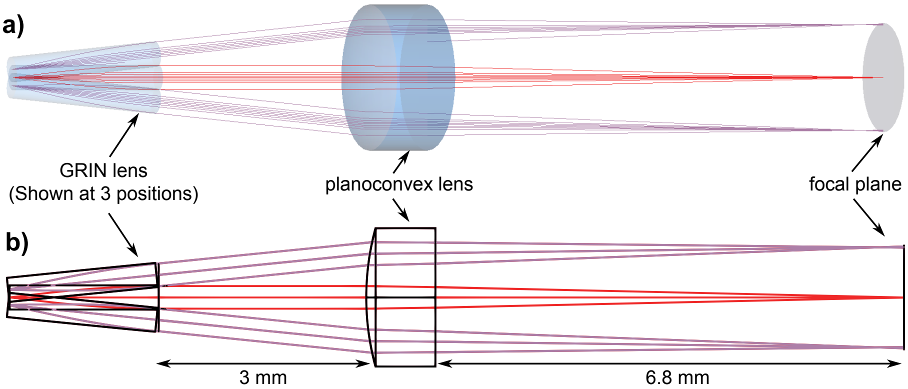

Figure 1.8: **a)** 3D ZEMAX raytracing of the OCT beam path for the center (red rays) and marginal (purple rays) position of the GRIN lens in the single modality demonstrator. **b)** Cross section of a).

The equivalence of both systems is reaffirmed by the similarity of their simulated MTF. Again, Figure 1.9 indicates that the single modality demonstrator is diffraction-limited.

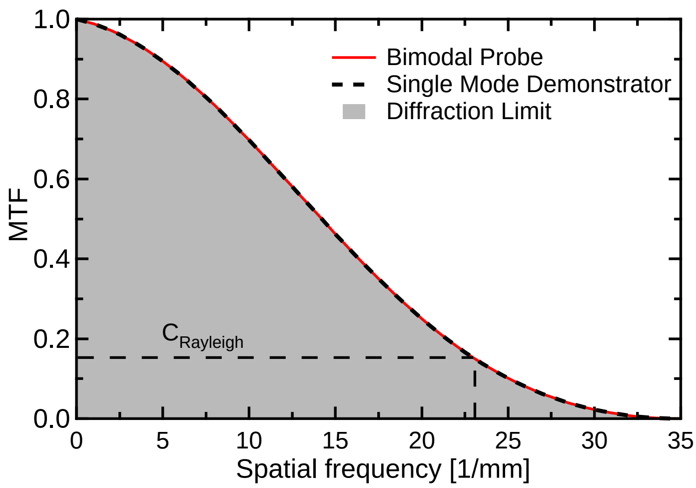

Figure 1.9: Simulated MTF curve of the OCT beam path for the bimodal probe and the single modality demonstrator. It can be seen that both implementations are optically equivalent and diffraction limited, providing a lateral resolution of 23.3 lp/mm or 43 µm.

Due to these similarities, it is expected that any experimental result obtained with the demonstrator can be easily transferred to the behavior of the bimodal probe.

1.3.6 Simulated Optical Performance

To conclude the *Design and Simulation* chapter, the most important characteristics of the components of the OCT microscope are listed in Table 1.1 and the simulated performance in Table 1.2.

Parameter	Value
Single mode fiber NA	0.18
GRIN lens NA	0.2
GRIN lens focal length	0.91 mm
Planoconvex lens focal length	7.5 mm

Table 1.1: Summary of the most relevant characteristics of the optical components used in the OCT modality.

Parameter	Bimodal Probe	Single Mode Demonstrator
Distal Side NA	0.022	0.022
Working Distance	7.3 mm	6.8 mm
Field of View	1.2 mm	1.5 mm
Depth of Field	3.4 mm	3.4 mm
Lateral Resolution	43 µm	43 µm

Table 1.2: Simulated optical performance and characteristics of the OCT modality. All resolution values follow the Rayleigh convention of 15.5% modulation [2].

1.4 Mechanical Design

In the following paragraphs the behavior of the fiber scanner is mechanically modeled, and this information used to choose the most relevant fabrication parameters.

The fiber scanner uses the concept of mechanical resonance to amplify 100-fold the subtle movement of the piezoelectric tube into a big displacement and angular deflection of the GRIN lens at the tip of the scanning fiber. Therefore, as in any resonant system, its geometrical and mechanical characteristics fully define the operating frequency range, and with it, constrain the way we can sample and acquire the final image.

As a resonant system, the movement of the scanning fiber is constrained to harmonic oscillations with a frequency close to $f_{\text{resonance}}$. If, for example, the scanner is moving in a circular pattern like in Figure 1.10 with period T, the number of sample points

$$N_T = \frac{f_{\text{sampling}}}{f_{\text{resonance}}} \tag{1.4}$$

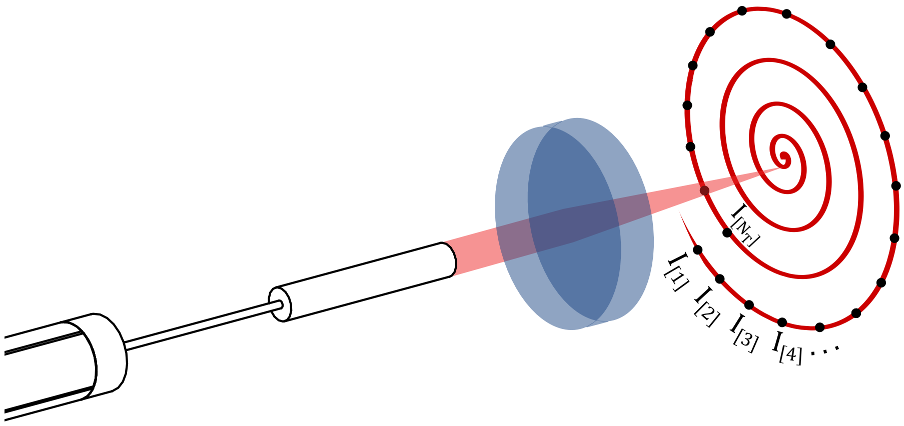

Figure 1.10: Schematic of the scanner focusing the OCT beam (red) in a plane. The beam describes a spiral trajectory to acquire an image. The N_T black dots represent the sampling points of the outermost ring of the spiral.

that can be acquired in this circle depend on the resonant frequency of the scanner and the sampling frequency of the OCT system.

As OCT systems have a relatively small sampling frequency (±100 kHz), we need to decrease the resonant frequency below 1 kHz to achieve more than 100 acquired point per ring of the spiral.

The following paragraphs describe how to calculate and reduce this frequency.

1.4.1 Resonant frequency calculation

Following Euler Bernoulli theory, the spring constant for a fixed-free, point loaded cantilever is given by

$$K_{\mathrm{cantilever}} = \frac{3EI}{L^3} = \frac{3\pi}{4}\frac{E_{\mathrm{fiber}} r_{\mathrm{fiber}}^4}{L^3} \tag{1.5}$$

considering that the moment of inertia of the cylindrical fiber is given by $I_{\mathrm{fiber}} = \frac{\pi}{4} r^4$.

The fiber-GRIN assembly can be modeled as a point-loaded, fixed-free cantilever and concentrating the weight of the GRIN lens in its center of gravity, as depicted in Figure 1.11). Now, by applying the ideal mass-spring harmonic resonator equation

$$f_{\mathrm{res}} = \frac{1}{2\pi}\sqrt{\frac{K_{\mathrm{cantilever}}}{m_{\mathrm{GRIN}}}} \tag{1.6}$$

it is possible to estimate the resonant frequency of the scanner. Note that, in order to assess the error of this approximation, we repeated the calculation of the resonant frequency using a more precise numerical method described in [3]. In the usable range of interest, the difference between the results from both methods

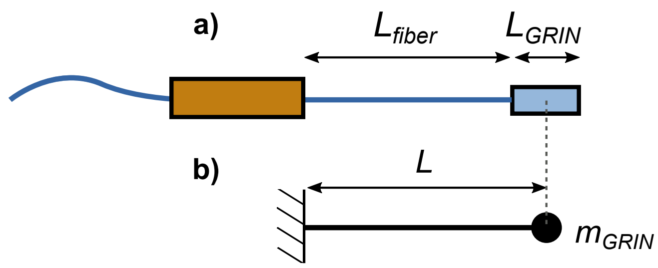

Figure 1.11: **a)** Drawing of the piezoelectricscanner: piezoelectric tube, fiber and GRIN lens. **b)** Simplified mechanical diagram obtained by modeling the fiber as a weightless cantilever and the GRIN lens as a point mass.

differed by less than 2%, indicating that Equation 1.6 is adequate for the modeling of the scanner.

As we can observe from equation 1.5 and 1.6, the resonance frequency increases quadratically with the diameter of the fiber. Therefore, by choosing a fiber with 80 µm instead of the standard 125 µm, the resonance frequency can be lowered from 1900 Hz to 770 Hz for a scanner with a total length of 4.5 mm.

The resonant frequency of a cantilever formed by a 80 µm fused silica fiber with the chosen GRIN lens is computed in Figure 1.12 using Equations 1.5 and 1.6.

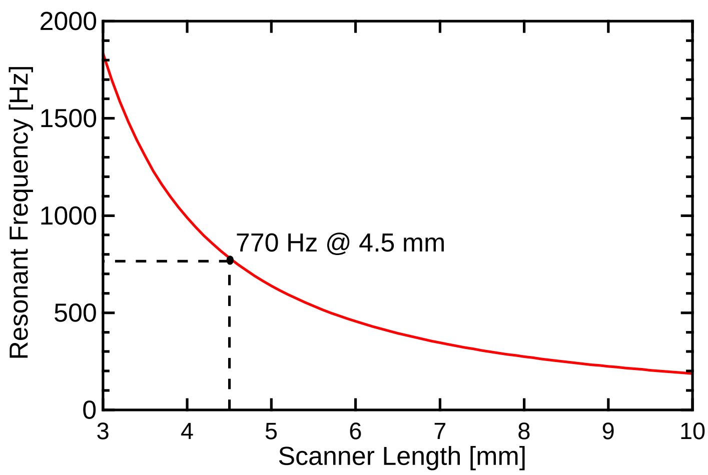

Figure 1.12: Resonant frequency of the scanner as a function of the scanning tip length (fiber + GRIN lens). The chosen working point is labeled in the plot.

As the scanner is buried in a 1 mm channel, the maximum displacement of the GRIN lens is limited to ±325 µm. Within that small displacement we want to achieve the maximum angular deflection of the GRIN lens to maximize the FOV, what can be achieved by using shorter fiber lengths. This shows a trade-off with the density of sampling N_{T}, which is increased with longer fiber lengths. To balance those terms, we chose a a total scanner length of 4.5 mm, with characteristics summarized in

Table 1.3.

Total scanner length	4.5 mm
Resonant Frequency	770 Hz
Max. angular deflection	5°

Table 1.3: Mechanical characteristics of the fiber scanner.

1.4.2 COMSOL simulation

In order to validate the theoretical analysis of the previous section, we performed a multiphysics finite element analysis using COMSOL. For that matter, the actuator was modeled as a radially polarized piezoelectric material (*PIC 151*) and the rest of the structure as elastic material. The excitation voltage is a sinusoidal symmetrical potential between the top and bottom electrodes of the tube.

As the system undergoes small deflections, it is simulated assuming linear behavior [4].

The first step is to simulate the resonant frequency of the system. Performing an *Eigenfrequency* study, we obtain a first mode resonance at 762 Hz, which closely matches our analytical estimation of 770 Hz. The mode shape at resonance is shown in Figure 1.13.

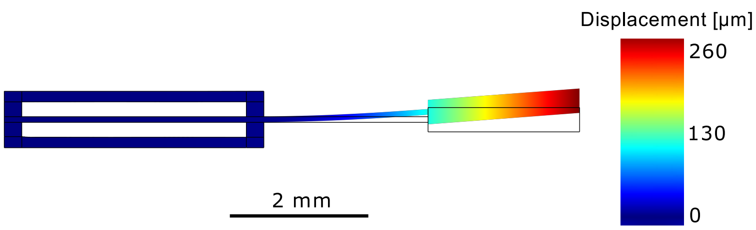

Figure 1.13: COMSOL simulation showing a cross section of the scanner at resonance at its maximum amplitude. The deformed structure is color coded showing the total displacement from the rest position (shown outlined). The base of the fiber (close to the actuator) is almost static, confirming the resonant behavior of the scanner.

Thanks to the multiphysics simulation, we can also check the electric field distribution inside the piezoelectric tube. As can be seen in Figure 1.14, for a symmetrical actuation in the left and right electrodes with a voltage of $\pm 75\,\mathrm{V}$, most of the volume under those electrodes experiences a field magnitude close to the expected theoretical value $E = U/d = 75\,\mathrm{V}/150\,\mu\mathrm{m} = 500\,\mathrm{V/m}$, which is under the safe operating field of *PIC 151*, ranging from $+1000\,\mathrm{V/m}$ to $-700\,\mathrm{V/m}$. Only some fringe areas exceed these values, which could become depolarized with time.

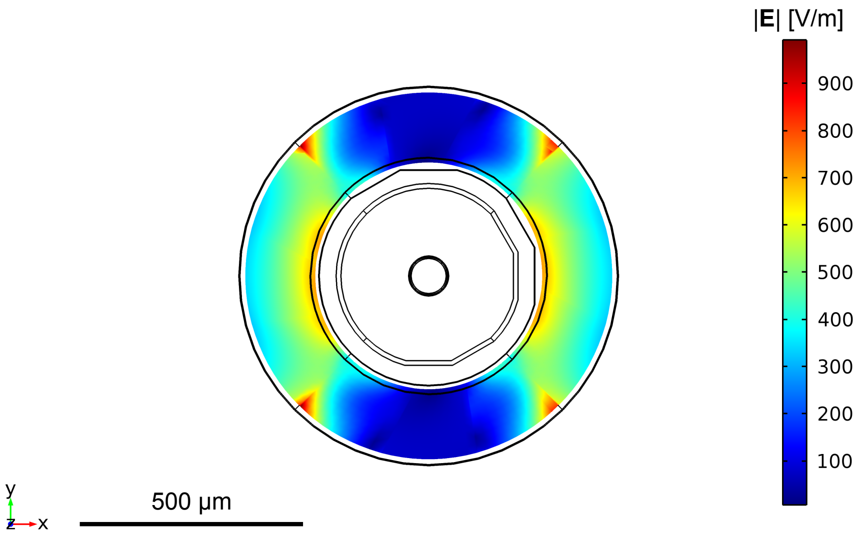

Figure 1.14: Magnitude of the electrical field inside a cross-section of the piezoelectric tube with an excitation voltage of $\pm 75\,\mathrm{V}$.

.

Bibliography

[1] H. D. Ford and R. P. Tatam, "Swept-source OCT with coherent imaging fibre bundles," vol. 7503, no. 0, pp. 18–21, 2009.

[2] S. Kretschmer, *Entwicklung einer bimodalen mikrooptischen Bank für endoskopische Anwendungen.* PhD thesis.

[3] L. Huo, J. Xi, Y. Wu, and X. Li, "Forward-viewing resonant fiber-optic scanning endoscope of appropriate scanning speed for 3D OCT imaging.," *Optics express*, vol. 18, no. 14, pp. 14375–14384, 2010.

[4] D. Fertis, "Basic Theories and Principles of Nonlinear Beam Deformations," *... and Methods to Solve Effectively Complex Nonlinear ...*, pp. 1–61, 2006.